

# UC San Diego

## International Symposium on Stratified Flows

### Title

Experimental study on periodically forced interfacial gravity waves in a rotating cylindrical basin

### Permalink

<https://escholarship.org/uc/item/3sn9j23m>

### Journal

International Symposium on Stratified Flows, 8(1)

### Authors

Rojas, Pedro

Ulloa, Hugo

Nino, Yarko

### Publication Date

2016-08-30

# Experimental study on periodically forced interfacial gravity waves in a rotating cylindrical basin

By Pedro Rojas <sup>1</sup>, Hugo Ulloa <sup>1,2</sup> & Yarko Niño <sup>1,3</sup>

Departamento de Ingenieria Civil, Universidad de Chile, pedrojas@ing.uchile.cl <sup>1</sup>  
Mechanical and Aerospace Engineering, University of California, hulloasanchez@eng.ucsd.edu <sup>2</sup>  
Advanced Mining Technology Center, Universidad de Chile, ynino@ing.uchile.cl <sup>3</sup>

## 1 Abstract

2 Diurnal wind-driven internal wave resonance regime, observed in stratified rotating lakes, was  
3 studied via laboratory experiments. The fundamental Kelvin wave (with a frequency  $\omega_K$ ) res-  
4 onance dynamics was forced in a homogeneous water layer, inside a cylindrical basin mounted  
5 on a turntable, with a frequency  $f/2$ , via a periodic forcing mechanism,  $\omega_w$ . The air-water  
6 interface displacement,  $\eta_\ell$ , simulated the internal interface response of an immiscible two-layer  
7 stratified basin forced by Coriolis and a diurnal wind phase. This was achieved by controlling  
8 the ratio of the Rossby radius of deformation to the cylindrical radius,  $R_\ell/R$ , the phase and  
9 the amplitude of a periodic forcing. Results showed strongly nonlinear wave dynamic regimes  
10 under idealized resonance conditions,  $\omega_w/\omega_K \equiv 1$ , on the shore, even for low energetic periodic  
11 forcings. Simultaneously, quasi-resonant states between other normal modes, such as Poincaré  
12 waves (with a frequency  $\omega_P$ ) and forcing sub-harmonics,  $n \omega_w$ , were identified in the offshore  
13 regions.

## 14 1 Introduction

15 The interaction between diurnal wind phase and the internal gravity wave field in stratified lakes  
16 can be understood as a forced harmonic oscillator system (Ockendon and Ockendon, 1973; Miles,  
17 1984). Horizontal momentum flux forced by the wind shear is balanced by barotropic and baro-  
18 clinic pressure gradients, disturbing thus the surface and internal interfaces of their equilibrium  
19 positions. During this process, a wide range of gravitational waves can be energized (Antenucci  
20 and Imberger, 2001). When the wind stops or becomes weaker in magnitude, the excited wave  
21 field propagates around the basin until damping mechanisms dissipate their energy (Shimizu  
22 and Imberger, 2009). However, the wind is typically periodic, so the interaction between wind  
23 and wave field can admit resonance regimes when the wind frequency (usually  $\omega_w = 2\pi/T_d$ , with  
24  $T_d = 24$  h) matches a fundamental frequency of the system (Antenucci and Imberger, 2003).  
25 Resonance interactions between wind forcing and large-scale gravitational waves have been iden-  
26 tified in stratified lakes (Rozas et al., 2014). Observations have shown that diurnal gentle winds  
27 can significantly amplify the modal amplitude of waves located close to the resonant frequency  
28 (Rozas et al., 2014). Additionally, resonant regimes can drive nonlinear wave dynamics, such  
29 as wave steepening, non-hydrostatic dispersion or sub-harmonics, allowing energy transfer from  
30 resonant modes to other modes (Boegman and Ivey, 2012).

31 There are not many experimental studies on resonantly forced basin-scale waves in non-  
32 rotating basins (Thorpe, 1974; Miles, 1984; Wake et al., 2007; Boegman and Ivey, 2012), but  
33 less attention has had the wind/wave resonant regime in rotating basins (Rozas et al., 2014). Un-  
34 derstanding resonant dynamic regimes and the quantification of the spatiotemporal distribution  
35 of the energy injected periodically by wind are key information to study transport processes in  
36 aquatic systems. The objective of this work is to study spatio-temporal dynamics of periodically  
37 forced gravity waves in rotating basins, as is the case of reservoirs or medium/large lakes located  
38 in extra/sub-tropical latitudes, respectively. These types of aquatic systems admit the existence  
39 of Kelvin and Poincaré waves (Csanady, 1967). In order to achieve this goal, laboratory exper-  
40 iments were conducted in a circular cylindrical acrylic tank mounted on a rotating turntable.  
41 Assuming that an  $n$ -layers stratified system can be expressed in  $n$  independent equations system

42 (Csanady, 1982; Stocker and Imberger, 2003), a one-layer system was adopted to emulate the  
 43 dynamic of the internal interface in a two-layer stratified fluid. This simplification does not  
 44 allow analyzing vertical mixing processes, but an adequate choice of rotation regime and the  
 45 aspect ratio between vertical and horizontal scales of the water body can scale the dynamics  
 46 of a stratified immiscible fluid. In this system, the waves spectrum is bounded by long gravity  
 47 waves, that scale with the diameter of the cylinder, and capillary waves. However, this study  
 48 focuses on the range of frequencies located between the fundamental Kelvin wave and nonlinear  
 49 high-frequency solitary waves (see e.g., de la Fuente et al., 2008; Ulloa et al., 2014).

50 The article is structured as follows: i) control parameters are defined; ii) experimental setup  
 51 and method are described; iii) results of time series (TS), power spectral density (PSD) and  
 52 wavelet transform (WT) of the air-water interface displacement are presented; iv) finally, results  
 53 are discussed in terms of background rotation, forcing frequency and space.

## 54 2 Theoretical formulation

55 Figure 1 shows an idealized cylindrical basin of radius  $R$ , with equivalent layer thickness  $h_\ell$   
 56 (Csanady, 1982), density  $\rho_\ell$ , inertial frequency  $f$  and vertical displacement of air-water interface  
 57  $\eta_\ell$ . The system is periodically forced by an amplitude  $\eta_0$  during a timescale  $t_{W_{on}}$  and is relaxed  
 58 during a timescale  $t_{W_{off}}$ , with a total time cycle of  $T_{tw} = t_{W_{on}} + t_{W_{off}}$ . The gravity wave field  
 59 dynamics has been controlled by two dimensionless parameters:

$$\mathcal{B} \equiv \frac{T_f}{T_g} = \frac{c_\ell T_f}{\lambda_h} , \quad \mathcal{F} \equiv \frac{T_K}{T_w} = \frac{\omega_w}{\omega_K} \quad (1)$$

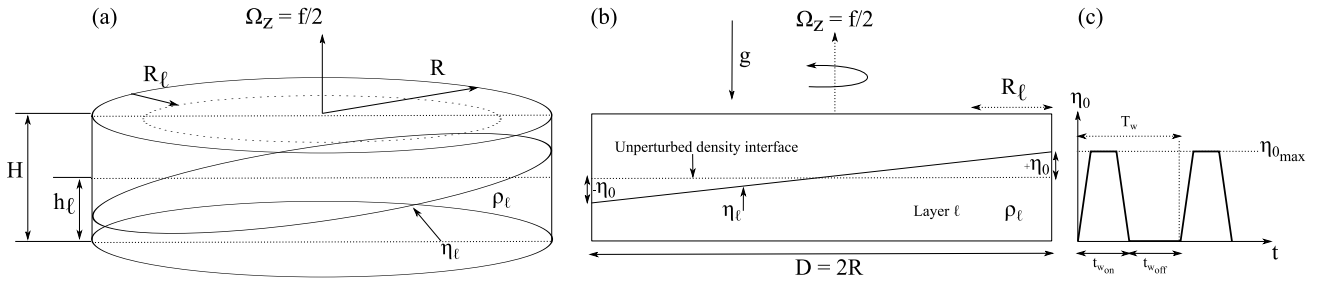


Figure 1: Conceptual model and controlled physical parameters.

60 The parameter  $\mathcal{B}$  controls the effect of rotation on large-scale gravity waves. Here  $T_f = 2\pi/f$   
 61 corresponds to the local inertial period, while  $T_g = \lambda_h/c_\ell$  is the characteristic time-scale of  
 62 gravity waves, where  $\lambda_h = 2\pi R$  is a horizontal length-scale and  $c_\ell = \sqrt{gh_\ell}$  is the linear speed  
 63 of the wave, with  $g$  the acceleration of gravity (Figure 1 a, b). Hence, this parameter can be  
 64 written as  $\mathcal{B} = R_\ell/R$ , where  $R_\ell = c_\ell/f$  is the internal Rossby radius of deformation. The  
 65 effect of rotation is more important in the dynamics of gravity waves as  $\mathcal{B} \rightarrow 0$ . Otherwise,  
 66 the rotation effect is weak or neglected when  $\mathcal{B} \rightarrow \infty$ . We refer to this number as the rotation  
 67 parameter or Burger number (Antenucci and Imberger, 2001).

68 The parameter  $\mathcal{F}$  compares the timescale of the natural period of the system (in this case,  
 69 the period of the fundamental Kelvin wave,  $T_K$ ) with the timescale of idealized forcing wind,  $T_w$   
 70 (Figure 1 c). As  $\mathcal{F} \rightarrow 1$ , resonance regimes are expected in the system. In a regime of perfect  
 71 resonance,  $\mathcal{F} \equiv 1$ , the energy is directly stored in the fundamental mode, inducing the increment  
 72 of the modal amplitude until it is controlled by both linear mechanisms (gravity and viscosity)  
 73 and nonlinear mechanisms (advection). Consequently, it is expected that the parameter  $\mathcal{F}$  also  
 74 affects the nonlinear dynamics of the gravity wave field.

75 Additionally, two other dimensionless parameters are used, which remain constant in all the  
 76 experiments. The first is the amplitude parameter  $\mathcal{A}_* \equiv \eta_{0,max}/h_\ell \equiv 0.15$ , and it defines the  
 77 maximum displacement of the forcing signal in terms of the ratio  $\mathcal{A}_* \equiv \eta_{0,max}/h_\ell$  (see Figure 1 c).

78 This parameter quantifies the work done by the wind to tilt the interface in a stationary regime.  
 79 This value has been chosen to represent regular observed conditions in internal interfaces of  
 80 two-layer stratified lakes (Antenucci and Imberger, 2003; Rozas et al., 2014). Although interface  
 81 vertical displacements can be much larger under extreme wind conditions, this study focuses on  
 82 exploring a 'normal' diurnal regime. The second parameter is associated with the wind phase  
 83 structure and it is defined as  $\mathcal{T}_w \equiv t_{W_{on}}/(t_{W_{on}} + t_{W_{off}}) \equiv 0.25$ . This parameter describes a  
 84 diurnal wind phase acting about 6 hours daily (e.g., Rozas et al., 2014).

85 It is important to note that linear normal modes (Kelvin and Poincaré waves) are obtained  
 86 solving the eigenvalue problem derived from the inviscid linear equations, in an f-plane (Csanady,  
 87 1967; Stocker and Imberger, 2003).

### 88 3 Experimental Setup

89 Laboratory experiments were performed in a cylindrical tank (180 cm of diameter and 50 cm  
 90 of depth) mounted on a turntable, whose angular velocity  $\Omega_z$  varies from 0 to 6 r.p.m. Figure  
 91 2 shows a schematic of the experimental setup. An electro-hydraulic control allows tilting and  
 92 releasing periodically an horizontal frame located between the cylindrical tank and the turntable,  
 93 in short times ( $t \approx 1$  s). The tank was filled with a water layer of thickness  $h_\ell = 0.05$  m and  
 94 density  $\rho_\ell \approx 1000$  kg/m<sup>3</sup>. Each experiment was conducted in two steps. First, the dimensionless  
 95 parameters controlled in each experiment,  $\mathcal{B}$  and  $\mathcal{F}$  were set. The rotation parameter was  
 96 achieved by spinning the turntable up until to get the inertial frequency  $f = 2 \Omega_z$  desired.  
 97 The forcing parameter was achieved by setting the values for the initial amplitude  $\mathcal{A}_*$  and the  
 98 temporal distribution of wind  $\mathcal{T}_w$ . Second, the basin was periodically tilted and released to  
 99 the horizontal position. This forcing induces a periodic adjustment of the air-water interface  
 100 in response to both the horizontal barotropic gradient and rotation, exciting periodically the  
 101 gravity wave field in the system.

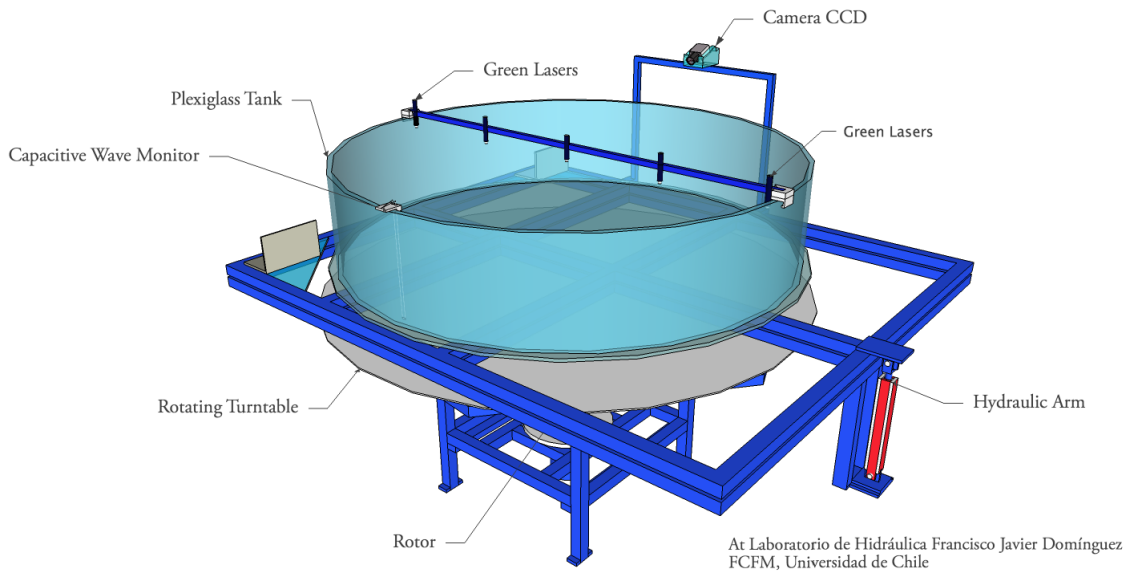


Figure 2: Schematic of the experimental setup.

102 The evolution of vertical displacement of the air-water interface was registered by combining  
 103 an optical method of laser-induced fluorescence and a capacitive type sensor, which allow us  
 104 to characterize the gravity wave field on both interior domain and boundary, respectively. For  
 105 the first method a fluorescent sheet was created (along the diameter periodically tilted) using  
 106 rhodamine to dye the water layer and a diametral green wavelength laser array (Figure 2). The  
 107 fluorescent sheet was registered at 25 Hz using a CCD that rotates with the system. For the

108 second method, a capacitive sensor (Churchill-Controls, model Wave Monitor) that sampled the  
 109 water level at 100 Hz was used to capture the interface in the boundary, where  $\eta_0(t=0, r \approx$   
 110  $0.98 R, \theta = -\pi/2) = 0$  (Figure 2). The set of experiments considered a total of 9 experiences,  
 111 spanning 3 values for the rotation parameter,  $\mathcal{B} = \{0.65, 1.00, 2.00\}$  and 3 values for the frequency  
 112 of the periodic forcing,  $\mathcal{F} = \{0.8, 1.0, 1.2\}$ . The periodic disturbance,  $\mathcal{A}_* = 0.15$  and temporal  
 113 distribution of wind  $\mathcal{T}_w = 0.25$  take constant values.

## 114 4 Results

115 Results of gravity wave field examined a sub-set of 6 experiments, considering 2 locations in the  
 116 space (Figures 3, 4 for  $r/R \approx 0.98$  and Figures 5, 6 for  $r/R \approx 0.40$ ), 2 rotation extreme regimes  
 117  $\mathcal{B} \in \{0.65, 2.00\}$  (moderate and weak rotation effect, respectively) and 3 forcing frequencies,  
 118  $\mathcal{F} \in \{0.8, 1.0, 1.2\}$ . Time series (TS) of the normalized interface displacement  $\eta_\ell/h_\ell$  and power  
 119 spectral density (PSD) of the  $\eta_\ell(t)/h_\ell$  are shown in Figures (3, 5), whereas wavelet transform  
 120 (WT) of  $\eta_\ell(t)/h_\ell$  are presented in Figures (4, 6).

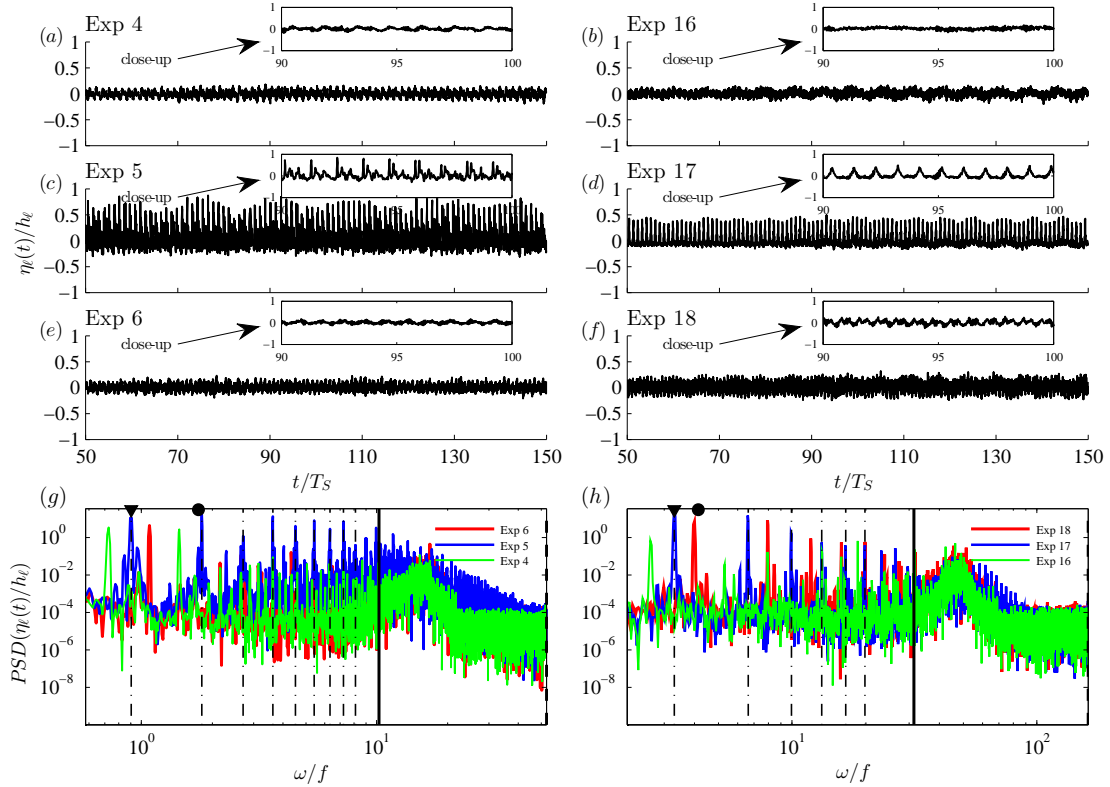


Figure 3: TS of interface displacement  $\eta_\ell(t, r \approx 0.98 R, \theta = -\pi/2) \pm \delta\eta_\ell$ , with  $\delta\eta_\ell \approx 2 \times 10^{-4}$  m. Experiments considered are:  $\mathcal{B} = 0.65 \pm 0.0014$  (a, c, e) and  $\mathcal{B} = 2.00 \pm 0.0007$  (b, d, f). The forcing frequencies for the respective rows are  $\mathcal{F} = 0.8 \pm 0.0016$  (a, b);  $\mathcal{F} = 1 \pm 0.0016$  (c, d);  $\mathcal{F} = 1.2 \pm 0.0016$ ; (e, f). Power spectral density (PSD):  $\mathcal{F} = 0.8 \pm 0.0016$ : green line;  $\mathcal{F} = 1.0 \pm 0.0016$ : blue line;  $\mathcal{F} = 1.2 \pm 0.0016$ : red line (g, h). Dot-dash line (·-) correspond to the first 9 sub-harmonics of the forcing frequency  $\mathcal{F} = 1.0 \pm 0.0016$ .  $\blacktriangledown$ : fundamental Kelvin wave frequency,  $\bullet$ : fundamental Poincaré wave frequency.

121 TS start at  $t \approx 50 T_S$ , where  $T_S = 4R/c_\ell$  is the period of the fundamental seiche. After  
 122  $t \approx 50 T_S$ , the gravity wave field is found in a pseudo-steady state. In addition, the wave  
 123 energy field in time/frequency space is calculated by wavelet transform technique (Torrence and  
 124 Compo, 1998) for  $90 < t/T_S < 100$ . Energy is normalized by the maximum energy observed at  
 125 the resonant forcing frequency ( $\mathcal{F} = 1.0$ ).

126 Both TS and PSD exhibit significant differences depending on the rotation and the forcing  
 127 frequency at  $r/R \approx 0.98$ . Higher amplitudes of  $\eta_\ell/h_\ell$  are observed in experiments in which

128  $\mathcal{F} = 1.0$  (Figure 3 *c, d*), in agreement with Rozas et al. (2014). In this resonant regime, basin-  
 129 scale waves show a strongly nonlinear degeneration along with the formation of solitary type  
 130 waves when  $\mathcal{B} = 0.65$  (moderate rotation). The nonlinear dynamic enhances the transfer of  
 131 energy from large to smaller scales (see close-up Figure 3 *c*). Energy peaks are observed at  
 132 harmonic frequencies of the primary forced mode (see dash-dot lines in Figures 3 *g, h*) for both  
 133 rotation regimes when  $\mathcal{F} = 1.0$  (blue lines of Figures 3 *g, h*). In addition, the PSD of moderate  
 134 rotation shows a wider energized normalized frequency bandwidth and higher energy peaks at  
 135 harmonics frequencies than the PSD of weak rotation (compare figures 3 *g* and 3 *h*).

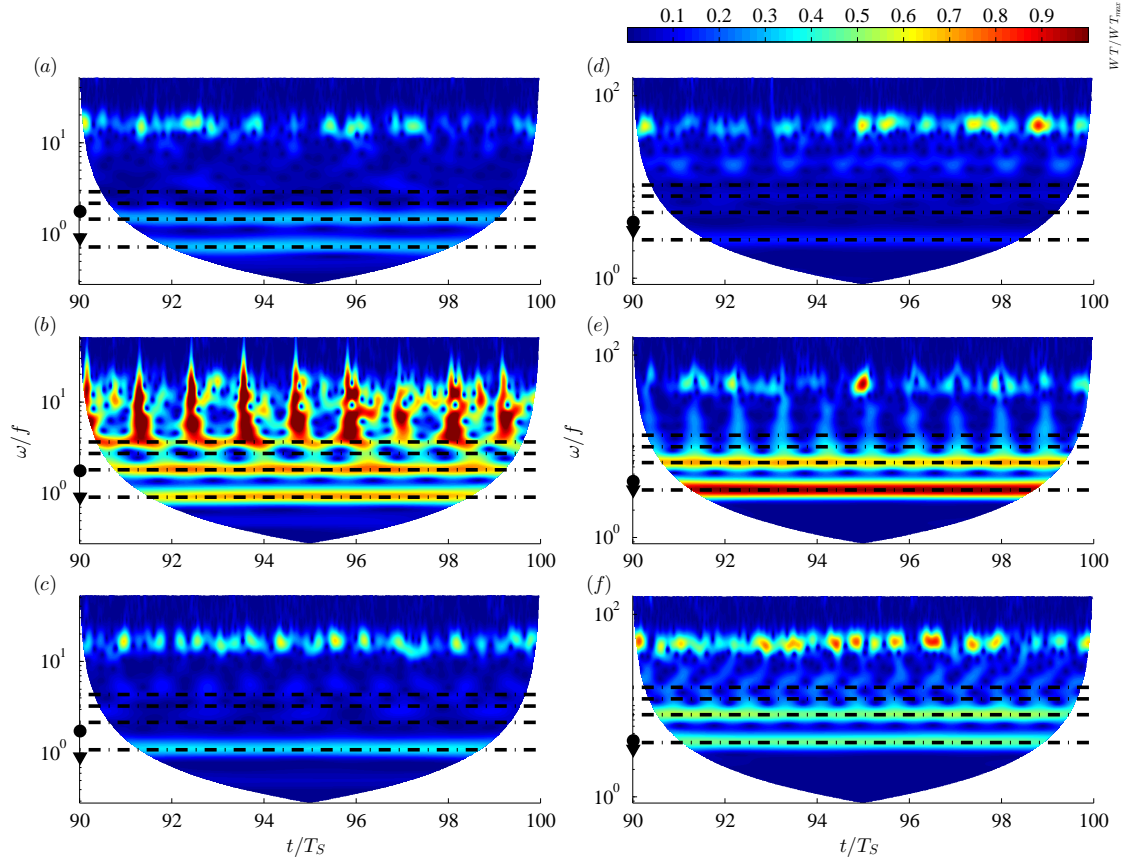


Figure 4: WT of the vertical displacement of the interface  $\eta_\ell(t, r \approx 0.98 R, \theta = -\pi/2) \pm \delta\eta_\ell$  with  $\delta\eta_\ell \approx 2 \times 10^{-4} \text{m}$ . Experiments considered are:  $\mathcal{B} = 0.65 \pm 0.0014$  (a, b, c) and  $\mathcal{B} = 2.00 \pm 0.0007$  (d, e, f). The forcing frequencies for the respective rows are:  $\mathcal{F} = 0.8 \pm 0.0016$  (a, d);  $\mathcal{F} = 1.0 \pm 0.0016$  (b, e);  $\mathcal{F} = 1.2 \pm 0.0016$ ; (c, f). Dot-dash lines (·-·) represent the first 4 sub-harmonic modes for each  $\mathcal{F}$  condition (from the bottom upwards).

136 High-frequency bandwidth is energized periodically ( $4 < \omega/f < 11$ ) due to energy transfer  
 137 driven by nonlinear processes, as  $\mathcal{F} \rightarrow 1$  and for a moderate rotation regime (Figure 4 *b*).  
 138 Furthermore, first and second harmonic modes (first and second horizontal dot-dash lines ·-·)  
 139 are periodically energized. Otherwise, absence of nonlinear processes lead to energy remains at  
 140 first harmonic, as  $\mathcal{F} \rightarrow 1$  and  $\mathcal{B} \approx 2$  (Figure 4 *e*). Moreover, sub-resonant and super-resonant  
 141 experiments (i.e  $\mathcal{F} = 0.8$  and  $\mathcal{F} = 1.2$ , respectively) show a different behavior only when the  
 142 effect of rotation is weak. Here, low and high frequencies have higher energy peaks with  $\mathcal{F} = 1.2$   
 143 (Figure 4 *f*).

144 Both TS and PSD exhibit clear differences in terms of rotating regime and the forcing fre-  
 145 quency at  $r/R \approx 0.40$ . Larger wave amplitudes are observed for weak rotating regime when  
 146  $\mathcal{F} = 0.8$  and  $\mathcal{F} = 1.2$  (Figures 5 *b, f*) and for moderate rotating regime when  $\mathcal{F} = 1.0$  (Figure 5  
 147 *c*). This can be understood in terms of the energy distribution as function of the Rossby radius  
 148 of deformation ( $R_\ell$ ). Weaker rotating regimes can store more potential energy than moderate ro-

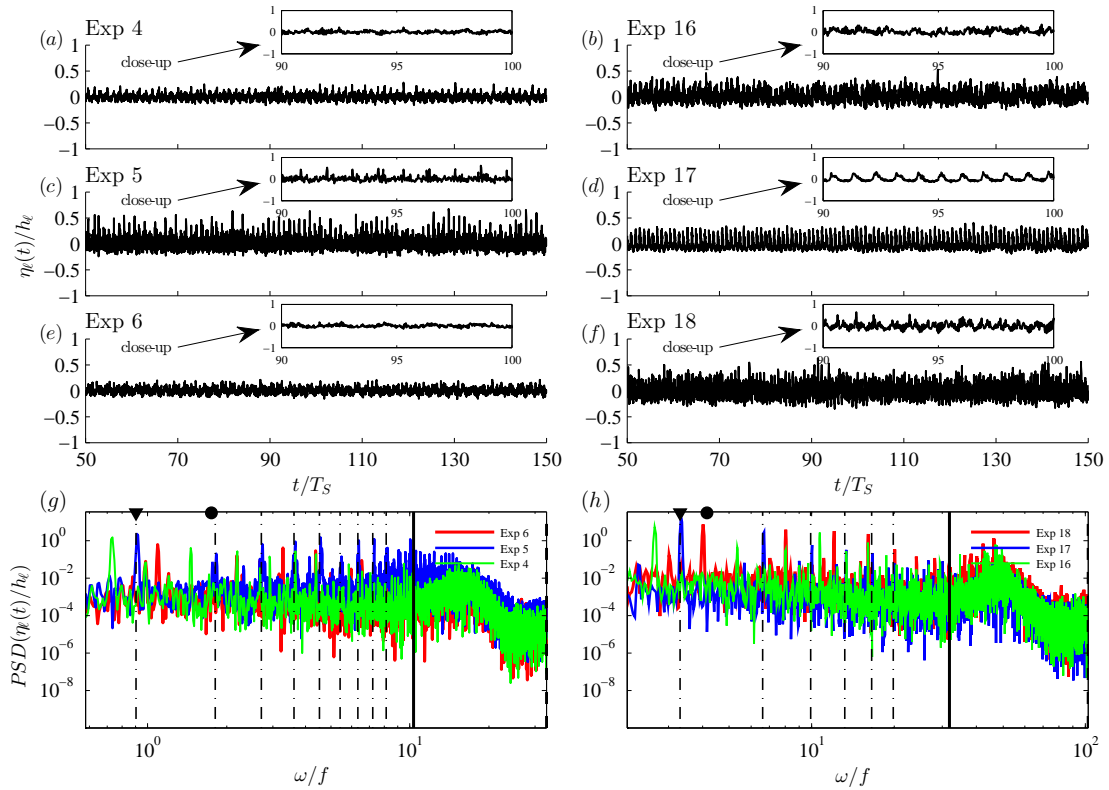


Figure 5: TS of interface displacement  $\eta_\ell(t, r \approx 0.40 R, \theta = 0) \pm \delta\eta_\ell$ , with  $\delta\eta_\ell \approx 2 \times 10^{-4}$ m. Idem Figure 3.

149 tating regimes within the Rossby radius of deformation (Antenucci and Imberger, 2001; Stocker  
 150 and Imberger, 2003), regardless the forcing frequency. Then, weaker rotations allow higher am-  
 151 plitudes in the interior. However, under stronger rotating regimes, the combination of nonlinear  
 152 wave dynamics and resonance forcing frequency (Figure 5 c) can lead to higher wave amplitudes.  
 153 Furthermore, regardless the rotating regime, nonlinear steepening processes are not longer ev-  
 154 ident in the interior domain. Energy peaks are observed at harmonics of the primary forced  
 155 mode (see dash-dot lines in Figures 5 g, h) for both rotation regimes with  $\mathcal{F} = 1.0$  (blue lines of  
 156 Figures 5 g, h). As is observed on the boundary ( $r/R \approx 0.98$ ), peaks show a different behavior  
 157 as a function of Burger number. For the weak rotation, high-frequency harmonic bandwidth is  
 158 narrower than the moderate rotation. In addition, the higher energy peak for both rotations is  
 159 located at the first harmonic (resonance state between the forcing and the fundamental Kelvin  
 160 wave  $\blacktriangledown$ ).

161 For a moderate rotation regime (Figure 6 b), the interior region ( $r/R \approx 0.40$ ) shows that  
 162 the high-frequency bandwidth ( $6 < \omega/f < 11$ ) is intermittently energized, following a complex  
 163 time pattern. This result suggests the existence of other nonlinear degeneration mechanisms  
 164 in the interior basin (Grimshaw et al., 2013), which are not necessary associated with nonlin-  
 165 ear processes driven by wave steepening. Moreover, both rotation regimes show that the first  
 166 harmonic is continuously energized in terms of time (see Figure 6), being more intense when  
 167 rotation is weak (first horizontal dot-dash lines  $\cdot -$  in Figure 6 d, e, f). Otherwise, sub-resonant  
 168 and super-resonant experiments (i.e.,  $\mathcal{F} = 0.8$  and  $\mathcal{F} = 1.2$ , respectively) exhibit a different  
 169 behaviour only when the effect of rotation is weak. Here, low and high frequencies have higher  
 170 energy with  $\mathcal{F} = 1.2$  (Figure 4 f). Finally, high-frequency energy is higher with respect to  
 171 energy observed at  $r/R \approx 0.98$  (Figure 6 d, f).

172



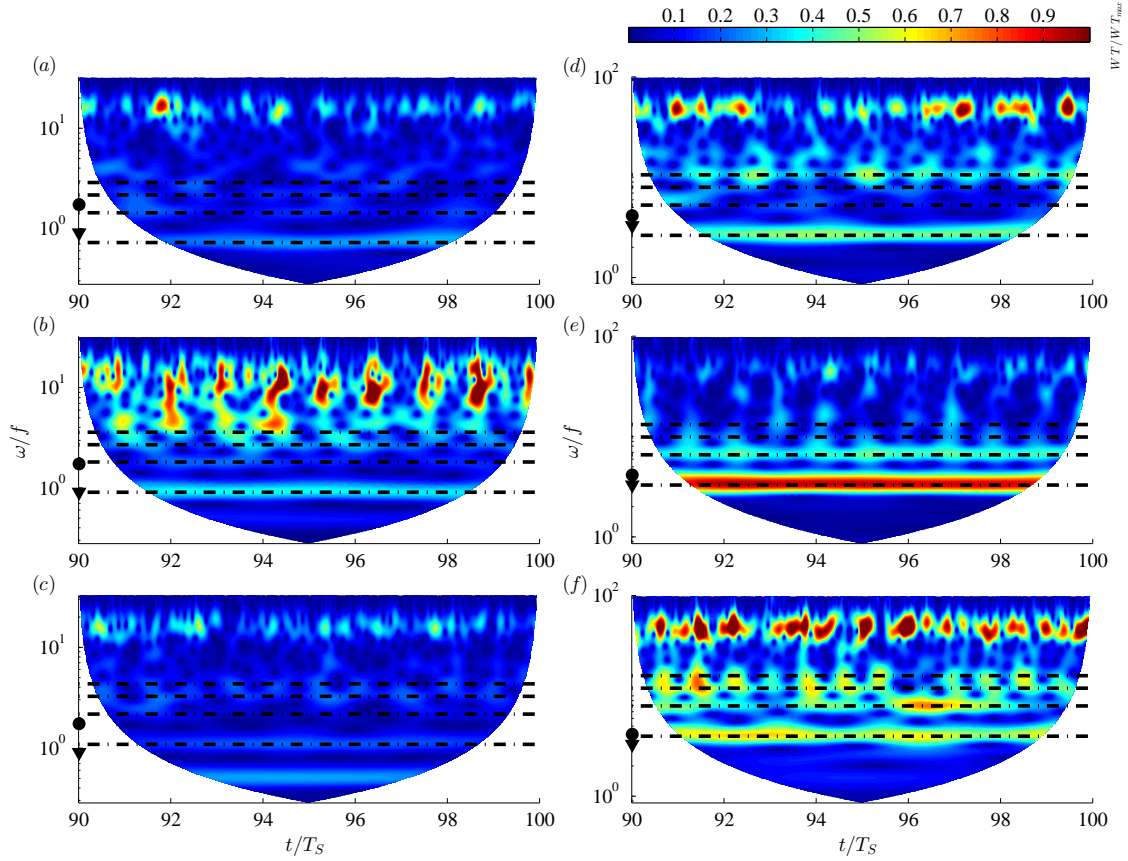


Figure 6: WT of the vertical displacements of the interface  $\eta_\ell(t, r \approx 0.40 R, \theta = 0) \pm \delta\eta_\ell$ , with  $\delta\eta_\ell \approx 2 \times 10^{-4} \text{m}$ . Idem Figure 4.

## 173 5 Discussion

174 In this work, laboratory experiments were conducted to study the spatiotemporal response of  
 175 a periodically forced fluid in an ambient where the rotation effect is not negligible, motivated  
 176 by field observations that showed resonance regime between the diurnal wind forcing and large-  
 177 scale gravitational waves (Antenucci and Imberger, 2003; Rozas et al., 2014). The results exhibit  
 178 similar resonance regime between the fundamental Kelvin mode ( $\blacktriangledown$ ) and the primary forced mode  
 179 (or first harmonic, with  $\mathcal{F} = 1$ ) observed previously by Rozas et al. (2014) in a rectangular  
 180 domain. The role of rotation in the nonlinear dynamic of boundary trapped large-scale waves is  
 181 robust and it has been studied in previous works (Sakai and Redekopp, 2010; Ulloa et al., 2014).  
 182 In this work we show that a quasi-steady nonlinear/non-hydrostatic wave regime is achieved  
 183 when the rotating flow is periodically forced at the resonance frequency,  $\mathcal{F} = 1$ , even for low  
 184 forcing magnitudes. Furthermore, there is a quasi-resonance state between the fundamental  
 185 Poincaré ( $\bullet$ ) wave and the first harmonic of the wind forcing, for  $\mathcal{F} = 1.2$  and weak rotation.  
 186 This result could explain the degeneration and spectral energy distribution at high-frequencies  
 187 in the interior basin (see Figure 6 *f*), as a consequence of other energy transfer mechanisms  
 188 associated to Poincaré waves, which could be independent of those nonlinear mechanisms that  
 189 drive the Kelvin wave degeneration. Furthermore, this pseudo-resonant state demonstrates the  
 190 higher energy contained at low frequencies as  $\mathcal{F} = 1.2$  with respect to  $\mathcal{F} = 0.8$ . The Poincaré  
 191 wave has a second pseudo-resonant regime with the second harmonic of  $\mathcal{F} = 1$  when  $\mathcal{B} = 0.65$ .  
 192 As  $r/R \rightarrow 0$ , the energy contained in this resonant regime is lower (see Figures 3; 5*g*) due to  
 193 the radial energy decay as a function of the Rossby radius of deformation. Further research is  
 194 required to quantify the effect of viscous dissipation in the resonance regime.



195 **References**

- 198 Antenucci, J. and Imberger, J. (2001). Energetics of long internal gravity waves in large lakes.  
199 *Limnol. Oceanogr.*, 46:1760–1773, doi:10.4319/lo.2001.46.7.1760.
- 200 Antenucci, J. P. and Imberger, J. (2003). The seasonal evolution of wind/internal wave resonance  
201 in lake kinneret. *Limnol. Oceanogr.*, 48(5):2055–2061, doi:10.4319/lo.2003.48.5.2055.
- 202 Boegman, L. and Ivey, G. N. (2012). The dynamics of internal wave resonance in periodically  
203 forced narrow basins. *J. Geophys. Res*, 117(C11):doi:10.1029/2012JC008134.
- 204 Csanady, G. T. (1967). Large-scale motion in the great lakes. *J. Geophys. Res.*, 72:4151–4162,  
205 doi:10.1029/JZ072i016p04151.
- 206 Csanady, G. T. (1982). On the Structure of Transient Upwelling Events. *J. Phys. Oceanogr.*,  
207 12:84–96, dx.doi.org/10.1175/1520--0485(1982)012<0084:OTSOTU>2.0.CO;2.
- 208 de la Fuente, A., Shimizu, K., Imberger, J., and Niño, Y. (2008). The evolution of internal  
209 waves in a rotating, stratified, circular basin and the influence of weakly nonlinear and nonhy-  
210 drostatic accelerations. *Limnol. Oceanogr.*, 53(6):2738–2748, dx.doi.org/10.4319/lo.2008.  
211 53.6.2738.
- 212 Grimshaw, R. H. J., Helfrich, K. R., and Johnson, E. R. (2013). Experimental study of the  
213 effect of rotation on large amplitude internal waves. *Phys. Fluids*, 25:056602, doi:10.1063/  
214 1.4805092.
- 215 Miles, J. W. (1984). Resonantly forced surface waves in a circular cylinder. *J. Fluid Mech.*,  
216 149:15–31, doi:10.1017/S0022112084002512.
- 217 Ockendon, J. and Ockendon, H. (1973). Resonant surface waves. *J. Fluid Mech.*, 59(02):397–413,  
218 doi:10.1017/S0022112073001618.
- 219 Rozas, C., de la Fuente, A., Ulloa, H., Davies, P., and Niño, Y. (2014). Quantifying the effect of  
220 wind on internal wave resonance in lake Villarrica, Chile. *Environ. Fluid Mech.*, 14 (4):849–  
221 871, doi:10.1007/s10652--013--9329--9.
- 222 Sakai, T. and Redekopp, L. G. (2010). A weakly nonlinear evolution model for long internal waves  
223 in a large lake. *J. Fluid Mech.*, 637:137–172, dx.doi.org/10.1017/S0022112010001114.
- 224 Shimizu, K. and Imberger, J. (2009). Damping mechanisms of internal waves in continuously  
225 stratified rotating basins. *J. Fluid Mech.*, 637:137–172, doi:10.1017/S0022112009008039.
- 226 Stocker, R. and Imberger, J. (2003). Energy Partitioning and Horizontal Dispersion  
227 in a Stratified Rotating Lake. *J. Phys. Oceanogr.*, 33:512–529, dx.doi.org/10.1175/  
228 1520--0485(2003)033<0512:EPAHDI>2.0.CO;2.
- 229 Thorpe, S. (1974). Near-resonant forcing in a shallow two-layer fluid: a model for the internal  
230 surge in loch new? *J. Fluid Mech.*, 63(03):509–527, doi:10.1017/S0022112074001753.
- 231 Torrence, C. and Compo, G. P. (1998). A practical guide to wavelet analysis. *Bulletin of the*  
232 *American Meteorological society*, 79(1):61–78, dx.doi.org/10.1175/1520--0477(1998)  
233 079<0061:apgtwa>2.0.co.
- 234 Ulloa, H. N., de la Fuente, A., and Niño, Y. (2014). An experimental study of the free evolution  
235 of rotating, nonlinear internal gravity waves in a two-layer stratified fluid. *J. Fluid Mech.*,  
236 742:308–339, dx.doi.org/10.1017/jfm.2014.10.
- 237 Wake, G. W., Hopfinger, E. J., and Ivey, G. N. (2007). Experimental study on resonantly  
238 forced interfacial waves in a stratified circular cylindrical basin. *J. Fluid Mech*, 582:203–222,  
239 doi:10.1017/S002211200700585X.